ARMY RESEARCH LABORATORY

Size Effects in Ceramic Materials: Computational Issues Associated With Parameter Estimations

by Stephen F. Duffy and Eric H. Baker

ARL-CR-0560 **April 2005**

prepared by

Connecticut Reserve Technologies, LLC
2997 Sussex Court
Stow, Ohio 44224

under contract

DAAD17-02-P-0503

NOTICES

Disclaimers

The findings in this report are not to be construed as an official Department of the Army position unless so designated by other authorized documents.

Citation of manufacturer's or trade names does not constitute an official endorsement or approval of the use thereof.

DESTRUCTION NOTICE—Destroy this report when it is no longer needed. Do not return it to the originator.

Army Research Laboratory
Aberdeen Proving Ground, MD 21005-5069

ARL-CR-0560 **April 2005**

Size Effects in Ceramic Materials: Computational Issues Associated With Parameter Estimations

Stephen F. Duffy and Eric H. Baker
Connecticut Reserve Technologies, LLC

REPORT DOCUMENTATION PAGE

Form Approved
OMB No. 0704-0188

1. REPORT DATE *(DD-MM-YYYY)*	2. REPORT TYPE	3. DATES COVERED (From - To)
April 2005	Final	April 2002 to July 2003

4. TITLE AND SUBTITLE

Size Effects in Ceramic Materials: Computational Issues Associated With Parameter Estimations

5a. CONTRACT NUMBER
DAAD17-02-P-0503

5b. GRANT NUMBER

5c. PROGRAM ELEMENT NUMBER

6. AUTHOR(S)

Stephen F. Duffy and Eric H. Baker (both of CRT, LLC)

5d. PROJECT NUMBER
622618.H80

5e. TASK NUMBER

5f. WORK UNIT NUMBER

7. PERFORMING ORGANIZATION NAME(S) AND ADDRESS(ES)

Connecticut Reserve Technologies, LLC
2997 Sussex Court
Stow, Ohio 44224

8. PERFORMING ORGANIZATION REPORT NUMBER
ARL-CR-0560

9. SPONSORING/MONITORING AGENCY NAME(S) AND ADDRESS(ES)

U.S. Army Research Laboratory
Weapons and Materials Research Directorate
Aberdeen Proving Ground, MD 21005-5066

10. SPONSOR/MONITOR'S ACRONYM(S)

11. SPONSOR/MONITOR'S REPORT NUMBER(S)

12. DISTRIBUTION/AVAILABILITY STATEMENT

Approved for public release; distribution is unlimited.

13. SUPPLEMENTARY NOTES

The contracting officer's representative (COR) is Jane W. Adams, U.S. Army Research Laboratory, ATTN: AMSRD-ARL-WM-MD, Aberdeen Proving Ground, MD 21005-5069, telephone number (410) 306-0865.

14. ABSTRACT

Two test specimen geometries obtained from circumferentially machined, tubular components have been proposed to investigate different flaw populations that might be present in a ceramic gun barrel. C-ring specimens tested in compression will generate maximum tensile stress states at the outer surface of the barrel. This stress state will activate critical flaws that are oriented parallel to the long axis of the tube. The sectored flexure bar specimen tested in four-point flexure will activate flaws aligned circumferentially around the tube. There is a need to take failure data from these tests and transform the information so that material characteristic strengths can be computed for subsequent Weibull analyses conducted on the gun barrel component. In order to compute the material characteristic strengths, the requisite Weibull effective area and/or effective volume parameters must be obtained. The procedure for numerically computing the Weibull effective area and effective volume for C-ring and sectored flexural test specimens is detailed in this article.

15. SUBJECT TERMS

ceramics; component design; parameter estimations; probability of failure

16. SECURITY CLASSIFICATION OF:			17. LIMITATION OF ABSTRACT	18. NUMBER OF PAGES	19a. NAME OF RESPONSIBLE PERSON
a. REPORT	b. ABSTRACT	c. THIS PAGE			Jane W. Adams
UNCLASSIFIED	UNCLASSIFIED	UNCLASSIFIED	SAR	35	19b. TELEPHONE NUMBER (*Include area code*) 410-306-0865

Contents

List of Figures

List of Tables

INTENTIONALLY LEFT BLANK

1. Introduction

Designing components fabricated from ceramic materials requires the capability to extrapolate failure statistics from test specimens to the components, i.e., one must be able to account for size effects commonly observed in ceramic material systems. The component of interest in this endeavor is a ceramic gun barrel. Before the program began, planning that supported this effort anticipated the need to capture defects spatially distributed around the circumference of the barrel, as well as defects spatially distributed down the length of the barrel. This focused attention on two types of test specimen geometries. Specifically, a C-ring geometry was adopted to investigate circumferential flaws, and a sectored flexure specimen subjected to four-point bending will be used to investigate longitudinally distributed flaws. A review of currently available analytical methods is presented for the C-ring specimen, and results from extensive computer modeling efforts are presented herein for both test specimen geometries. The test specimen geometries were defined by the U.S. Army Research Laboratory (ARL), and the intent was to determine the effective volume and effective area (respectively referred to as $k_V \cdot V$ and $k_A \cdot A$ in the ceramics literature) as a function of the Weibull modulus and geometry. Here, the k_V and k_A are stress gradient factors, and V and A are gauge volume and gauge area, respectively. Calculation of $k_V \cdot V$ and $k_A \cdot A$ required numerical computations using both finite element analysis and Weibull analysis. The ANSYS[1] finite element program was used to generate stress results for this effort, while the National Aeronautics and Space Administration Glenn Research Center Ceramics Analysis and Reliability Evaluation of Structures (CARES)/Life algorithm was used to conduct Weibull analyses.

2. Effective Volumes and Areas Using Finite Element Analysis

If the random variable representing uniaxial tensile strength of an advanced ceramic is characterized by a two-parameter Weibull distribution, then the failure probability for a test specimen fabricated from this advanced ceramic is given by the cumulative distribution function

$$P_f = 1 - exp\left[-\left(\frac{\sigma_{max}}{\sigma_\theta} \right)^m \right] \quad \sigma_{max} > 0 \tag{1}$$

$$P_f = 0 \quad \sigma_{max} \leq 0 \tag{2}$$

[1] ANSYS®, which is not an acronym, is a registered trademark of ANSYS, Inc.

in which

P_f = the probability of failure

σ_{max} = maximum uniaxial tensile stress in a test specimen at failure

σ_θ = the Weibull characteristic strength

m = Weibull modulus

Note that the Weibull characteristic strength depends on the geometry of the test specimen. In addition, the Weibull characteristic strength has units of stress. Strength-controlling flaws can be spatially distributed over the volume, the surface area, or edge length (three-, two-, or one-dimensional entities, respectively) of a test specimen. If the strength-controlling flaws are spatially distributed over the volume of the test specimen, the characteristic strength typically is designated as $(\sigma_\theta)_V$, and the Weibull modulus is typically designated as m_V. If the strength-controlling flaws are spatially distributed over the area of the test specimen, the characteristic strength is designated as $(\sigma_\theta)_A$, and the Weibull modulus is designated as m_A. If the strength-controlling flaws are distributed over the edge of a test specimen, then the characteristic strength is designated as $(\sigma_\theta)_L$, and the Weibull modulus is designated as m_L. It has been recognized for several decades that edge-based strength-limiting flaws in ceramics can be particularly debilitating to failure stress. Typically, edges in ceramic specimens and components are chamfered or rounded for that reason (i.e., surface- and volume-based flaws are controlling); however, edge alteration is not always practical in some applications, so the probability of failure attributable to these defects must be accounted for. Obviously, for tubular or rounded specimens and components, the consideration of edge-based strength-limiting flaws is not necessary.

An alternate expression for the probability of failure is given by

$$P_f = 1 - \exp\left[-\int_V \left(\frac{\sigma}{(\sigma_0)_V} \right)^{m_V} dV \right] \qquad \sigma > 0 \tag{3}$$

$$= P_f = 0 \qquad \sigma \le 0 \tag{4}$$

The integration within the exponential function is performed over all tensile regions of the specimen volume if the strength-controlling flaws are randomly distributed through the volume of the material. The integration is sometimes performed over an effective gauge section instead of over the total volume of the test specimen. In equation 3, m_V is the Weibull modulus associated with strength-controlling flaws distributed through the volumes of the specimens. Also in equation 3, $(\sigma_0)_V$ is the Weibull material scale parameter and can be described as the Weibull characteristic strength of a specimen with unit volume loaded in uniform uniaxial tension. The Weibull material scale parameter has units of stress·(volume)$^{1/m_V}$ when the strength-controlling flaws are distributed through the volume of the material.

At this point, we assume that the Weibull modulus can be obtained from the failure data. Thus, in equation 3 we take

$$m_V = \tilde{m}_V \tag{5}$$

in which the tilde signifies that the value of m_V is an estimate obtained from failure data, and we identify

$$(\sigma_0)_V = \sigma^* \tag{6}$$

as a parameter; then

$$P_f = 1 - \exp\left[-\int_V \left(\frac{\sigma}{\sigma^*} \right)^{\tilde{m}_V} dV \right] \tag{7}$$

Rearranging yields

$$P_f = 1 - \exp\left[-\left(\frac{\sigma_{\max}}{\sigma^*} \right)^{\tilde{m}_V} \int_V \left(\frac{\sigma}{\sigma_{\max}} \right)^{\tilde{m}_V} dV \right] \tag{8}$$

Now let

$$k_V \cdot V = \int_V \left(\frac{\sigma}{\sigma_{\max}} \right)^{\tilde{m}_V} dV \tag{9}$$

in which V can be identified as the specimen gauge volume. Then

$$P_f = 1 - exp\left[-k_V \cdot V \left(\frac{\sigma_{max}}{\sigma^*} \right)^{\tilde{m}_V} \right] \tag{10}$$

Finally, solve equation 10 for the effective volume, $k_V \cdot V$. For the time being, treat σ^* as a parameter.

$$k_V \cdot V = \frac{-\ln\left(1 - P_f\right)}{\left(\frac{\sigma_{\max}}{\sigma^*} \right)^{\tilde{m}_V}} \tag{11}$$

At this point, we have outlined the theory that supports an approach that could use finite element analysis and Weibull analysis to evaluate the effective volume, $k_V \cdot V$, for a given specific test specimen geometry. The following steps are necessary to evaluate $k_V \cdot V$:

1. Estimate $\tilde{m}_V$ from failure data. In the case of the parametric study presented later, a range of values was assumed for $\tilde{m}_V$.

2. Use finite element analysis and Weibull analysis to numerically evaluate the following expression for a given specimen geometry from equation 7:

$$P_f = 1 - \exp\left[-\int_V \left(\frac{\sigma}{\sigma^*} \right)^{\tilde{m}_V} dV \right] \tag{7}$$

Here, $\tilde{m}_V$ from step 1 is used with an arbitrarily selected value of σ^*. Weibull analysis will numerically determine P_f for the (arbitrary) magnitude of the load applied to the specimen.

3. With σ^*, P_f, and σ_{max} (obtained from the finite element analysis), solve the following expression from equation 11:

$$k_V \cdot V = \frac{-\ln\left(1 - P_f\right)}{\left(\frac{\sigma_{\max}}{\sigma^*}\right)^{\tilde{m}_V}} \tag{11}$$

Note that an increase in the applied load will increase both P_f and σ_{max} so that $k_V \cdot V$ remains constant for a given specimen geometry. In addition, changing σ^* will affect the value of P_f obtained from step 2 so that $k_V \cdot V$ remains constant for a given material characteristic strength. The only parameter other than the geometry that will affect the value of $k_V \cdot V$ is the Weibull modulus $\tilde{m}_V$.

3. Finite Element Analysis of the C-Ring Specimen

In this section and several sections that follow, the methods of calculating the effective volume and area from finite element modeling for the C-ring specimen geometry are compared with calculations obtained with the published closed form solutions provided by Jadaan et al. (1991) and presented in American Society for Testing Materials (ASTM) C-1323. Throughout this report, the solution in Jadaan et al. (1991) will be referred to as the closed form solution. For this project, the C-ring geometry ideally has an outside diameter (OD) of 33 mm and an inside diameter (ID) of 24 mm. The specimen length for the C-ring was 8 mm, but several other lengths (specifically 2 mm and 4 mm) were examined to indicate certain analytical trends. Finite element analysis provides a numerical approximation of the stress field and the geometry of a component being analyzed. Since the probability of failure depends on stress and geometry, a mesh sensitivity study was conducted for the C-ring geometry provided. Five meshes were analyzed. These meshes and the corresponding number of elements are identified as follows:

1. Most coarse mesh: 864 elements
2. Coarse mesh: 2,800 elements
3. Coarse to medium mesh: 6,860 elements
4. Medium mesh: 16,128 elements
5. Fine mesh: 19,872 elements

The most coarse mesh and the most refined mesh appear in figures 1 and 2.

ANSYS SOLID95[2] elements were used to model the C-ring. A series of simulations was conducted on the ARL specimen geometry with the meshes cited previously. Force and displacement boundary conditions were imposed at the top of the C-ring. For a given specimen geometry, both approaches yielded identical results. In this report, displacement models are presented.

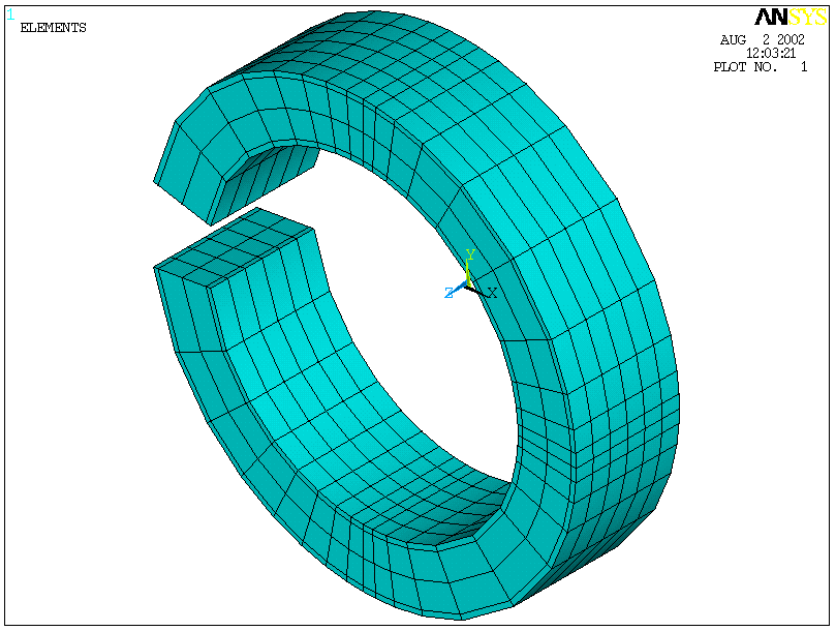

Figure 1. Most coarse C-ring mesh.

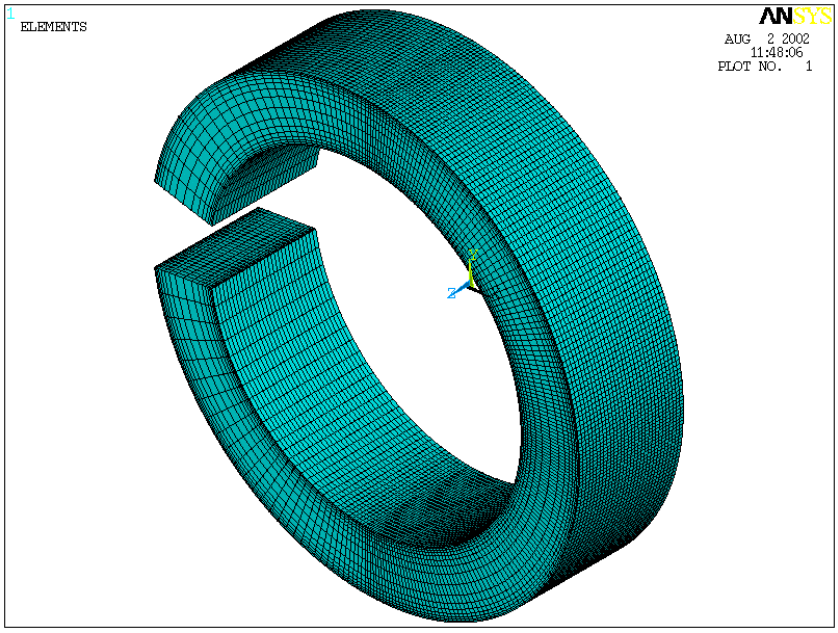

Figure 2. Most refined C-ring mesh.

[2]SOLID95 is a higher order version of the 3-D eight-node solid element SOLID45. It can tolerate irregular shapes without as much loss of accuracy.

The first principal stress contour plot for the ARL specimen geometry is depicted in figure 3. This contour plot is representative of the five meshes cited before. Although the magnitude of the first principal stress is not of consequence to this discussion, the distribution of the stresses is. Note the distinct parabolic distribution of stress along the length of the C-ring in figure 3.

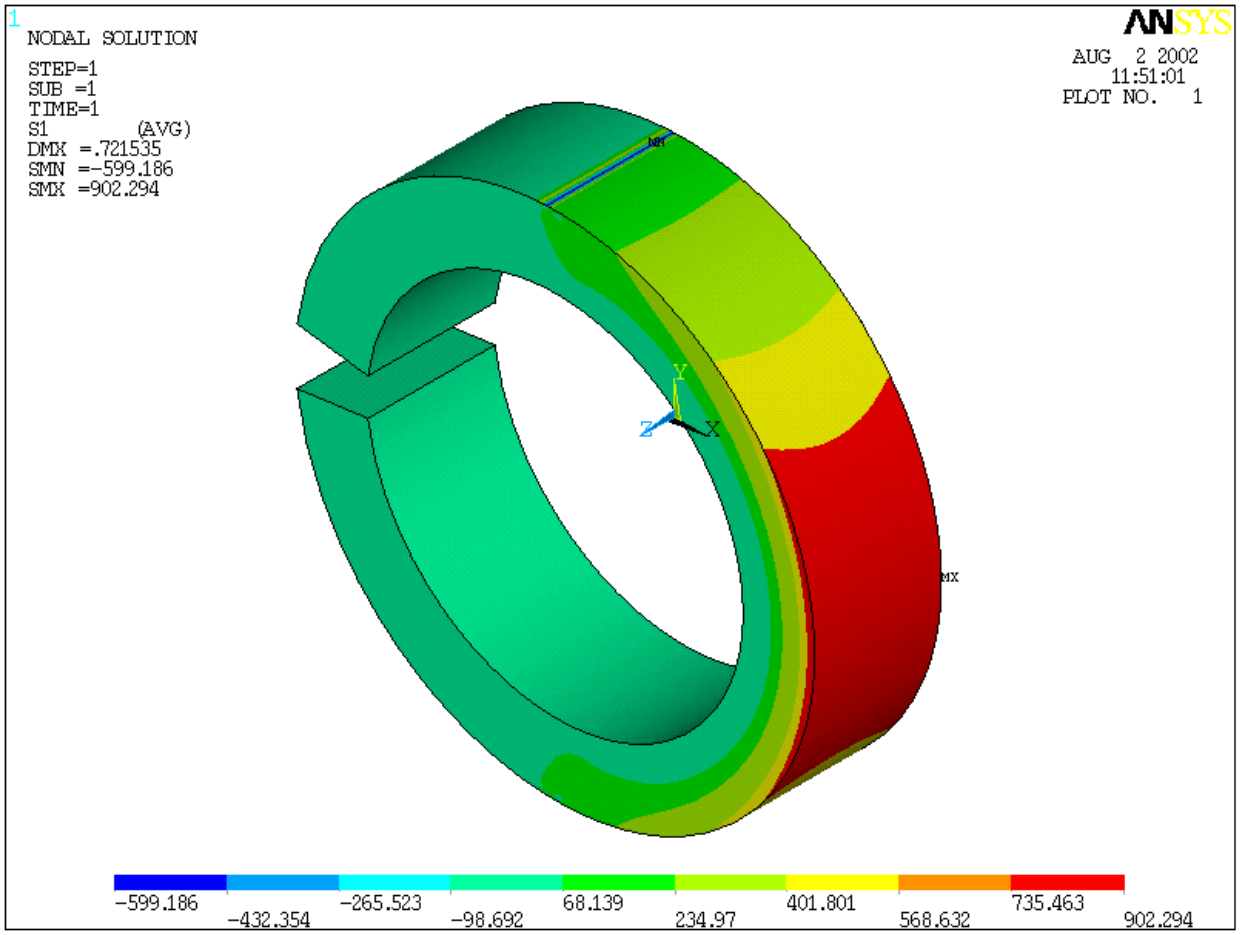

Figure 3. Principal stress contour map.

From the closed form solution, the maximum tensile stress (which occurs at the outer surface of the bend face) of a C-ring with an applied compressive load is given in this article as

$$\sigma_{\max} = \frac{P}{bt}\frac{R}{r_o}\left(\frac{r_o - r_a}{r_a - R}\right) \tag{12}$$

in which

P = load

t = radial thickness

b = length

r_o = outside radius

r_a = average radius

r_i = inner radius

and

$$R = \frac{r_o - r_i}{ln\left(\frac{r_o}{r_i}\right)} \tag{13}$$

A schematic drawing depicting the various geometries identified is provided in figure 4.

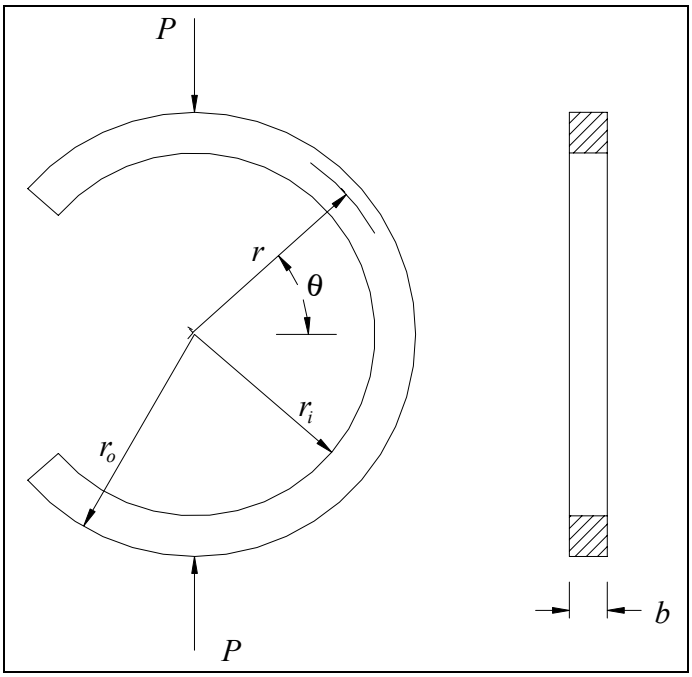

Figure 4. Schematic of C-ring specimen geometry.

An elasticity solution is also available (see Timoshenko and Goodier, 1970). The stress equation obtained from the elasticity solution has never been used to compute effective volumes or areas for the C-ring geometry. The elasticity equations are presented here for verification purposes only.

The strength of materials solution and the elasticity solution are two-dimensional solutions, i.e., the solutions are correct in the limit as the length of the C-ring approaches zero. Jadaan et al. (1991) assumed that this solution was valid through the length of the C-ring in order to derive closed form solutions for $k_V \cdot V$ and $k_A \cdot A$. This assumption is valid during limiting geometric constraints. Figure 5 depicts the variation of the maximum stress along the length of several C-rings for a number of values of $b/(r_o - r_i)$.

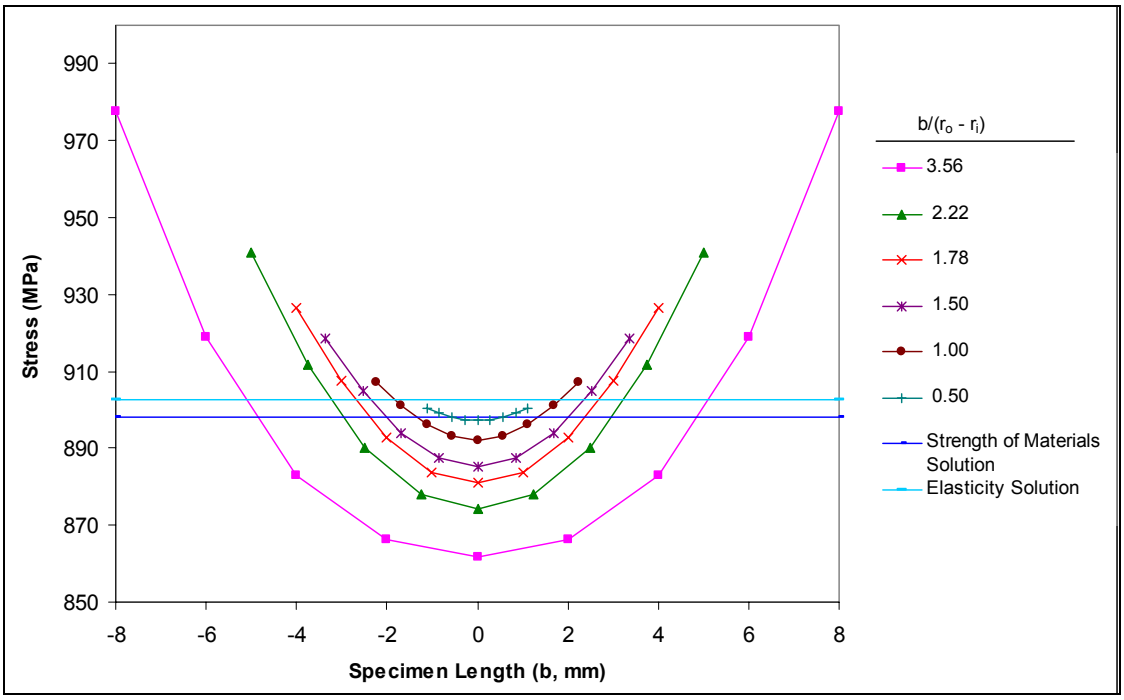

Figure 5. Maximum circumferential tensile stress as a function of specimen geometry.

The trend to a uniform stress distribution is readily apparent in figure 6. Here, the stress results are presented as a function of normalized (with respect to b) position along the length of the bend face.

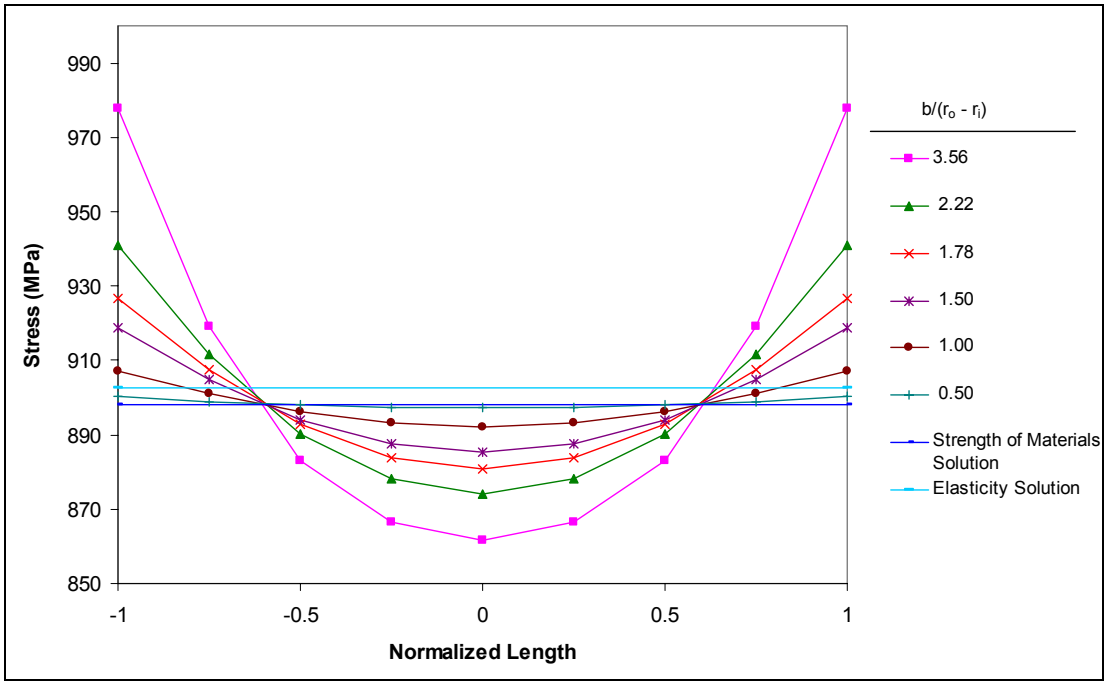

Figure 6. Maximum circumferential tensile stress as a function of specimen geometry normalized with respect to specimen length.

Clearly, the uniform stress distribution is not satisfied until

$$\left(\frac{b}{r_o - r_i}\right) \leq 0.5 \tag{14}$$

This result has practical implications for the testing community. The ARL C-ring geometry was designed to comply with geometric constraints specified in ASTM C-1323 in which

$$1 \leq \left(\frac{b}{r_o - r_i}\right) \leq 4 \tag{15}$$

The ARL C-ring geometry has a length-to-thickness ratio of 1.78 (in which b = 8 mm was specified and the inner and outer diameters could not be adjusted), which falls within the recommended limit suggested by the ASTM standard. From the stress results presented in figure 4, we feel that the ASTM C-28 committee should revisit this recommendation. If the inequality cited in equation 15 has practical testing implications (specimen alignment, stability, etc.), then a caveat should appear within the standard that states the expressions for $k_V \cdot V$ and $k_A \cdot A$ in the standard are in appreciable error.

4. Finite Element Analysis of the Sectored Flexure Specimen

The sectored flexure bar geometry was based on a tube with dimensions of 33 mm OD, 24 mm ID, and 100 mm length. The four-point bend test geometry consisted of an outer support span of 80 mm and an inner load span of 40 mm. The cross section of the contoured specimen was a 45-degree sector machined from the tube geometry (see figure 7).

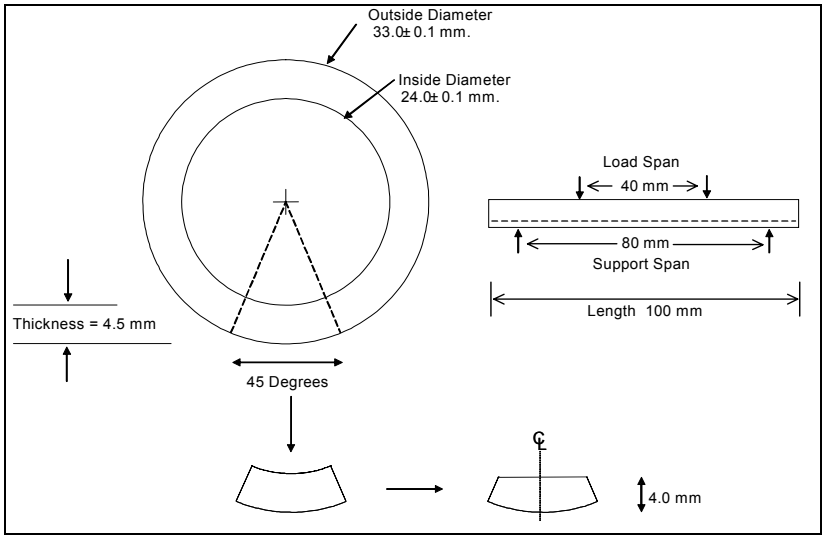

Figure 7. Sectored tube geometry.

A flat surface was machined on the compressive side of the contoured flexure specimen, producing a specimen with a maximum thickness of 4 mm. Bottom support fixtures (see figure 8) were assumed to have of an "hourglass" shape with the same radius of curvature as the contoured flexure specimen, promoting line loading which was modeled via finite element analysis.

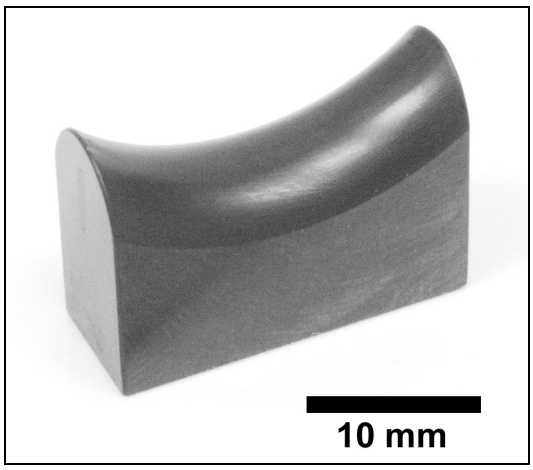

Figure 8. One of two contoured support fixtures (courtesy of S. Goodrich at the University of Dayton Research Institute).

Initially, models that have force and displacement boundary conditions imposed at the inner load supports were considered. The inner load supports are situated along the top of the specimen 40 mm apart (as depicted in figure 7). The force boundary conditions (outlined in red) are depicted in figure 9, which represents a model of the entire test specimen geometry. The hourglass supports for the bottom of the specimen are depicted in light blue.

For the applied displacement model, a displacement of 0.1 mm was imposed on all nodes across the top of the model at the inner supports. Unfortunately, unwarranted stresses were induced when this uniform displacement was applied.

The stresses corresponding to one of these lines of displaced nodes are depicted in figure 10. Nodes near the centerline (relative to x-axis) of the specimen exhibited compressive σ_y stresses (denoted as SY in the figure and by ANSYS) which were expected because of the compressive nature of the loading at these nodes. However, the σ_y stresses became tensile near the edges of the cross section. This indicates that these near-edge nodes sought to displace farther than the applied displacement of 0.1 mm and were actually "held back" by the proscribed displacement, thereby causing tensile stresses. Basically, the model's top surface has a tendency to curl down at the edges. The geometry associated with this curl cannot be calculated *a priori*. This strongly points to the use of contact stress elements in order to model the test specimen during displacement conditions. The use of contact stress elements was outside the present work scope, so attention was focused on modeling the test specimen by force boundary conditions.

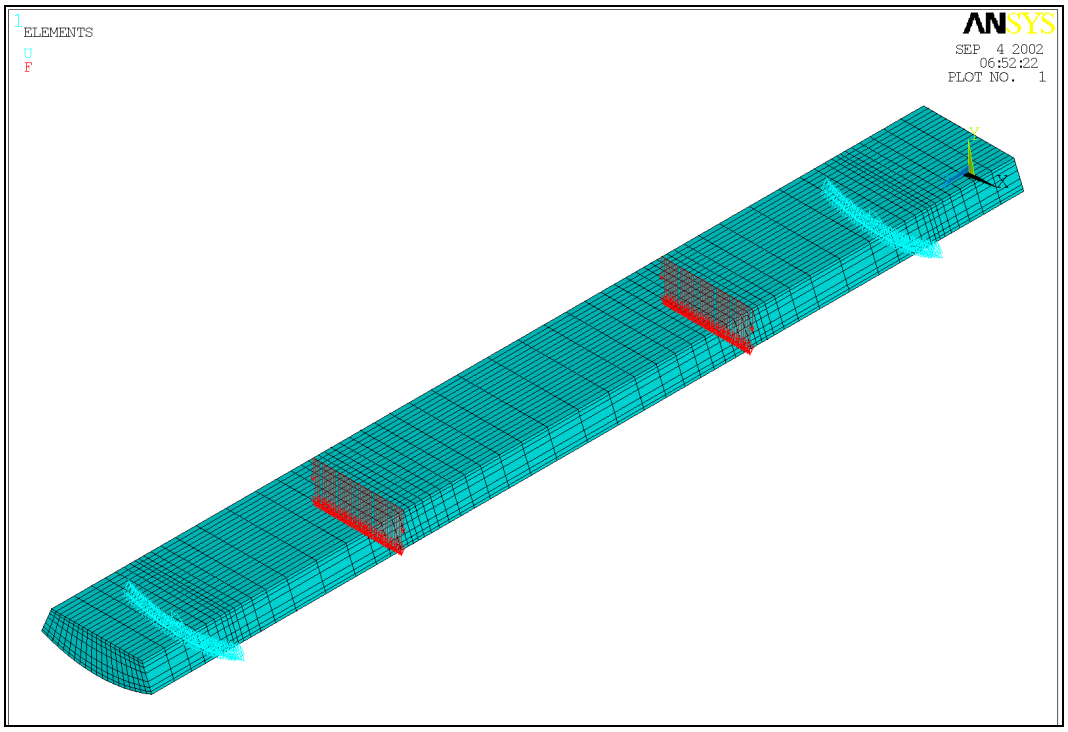

Figure 9. Full model with applied forces.

To ensure that the force boundary conditions model was behaving as expected, displacements were monitored at several locations in the model. These displacements were found to be consistent with a component undergoing four-point bending, and the decision was made to ascertain $k_V \cdot V$ and $k_A \cdot A$ via applied force models. Thus, the results presented in the remainder of the report represent finite element models with applied force boundary conditions.

Once the boundary conditions for the force model were established and verified, the stress state obtained from the finite element analysis was verified. A strength-of-materials solution was adopted for the closed form solution of the maximum tensile stress (which occurs at the outer surface of the bend face) in order to make this comparison. The closed form stress is given by the expression

$$\sigma_{max} = \frac{Mc}{I} \tag{16}$$

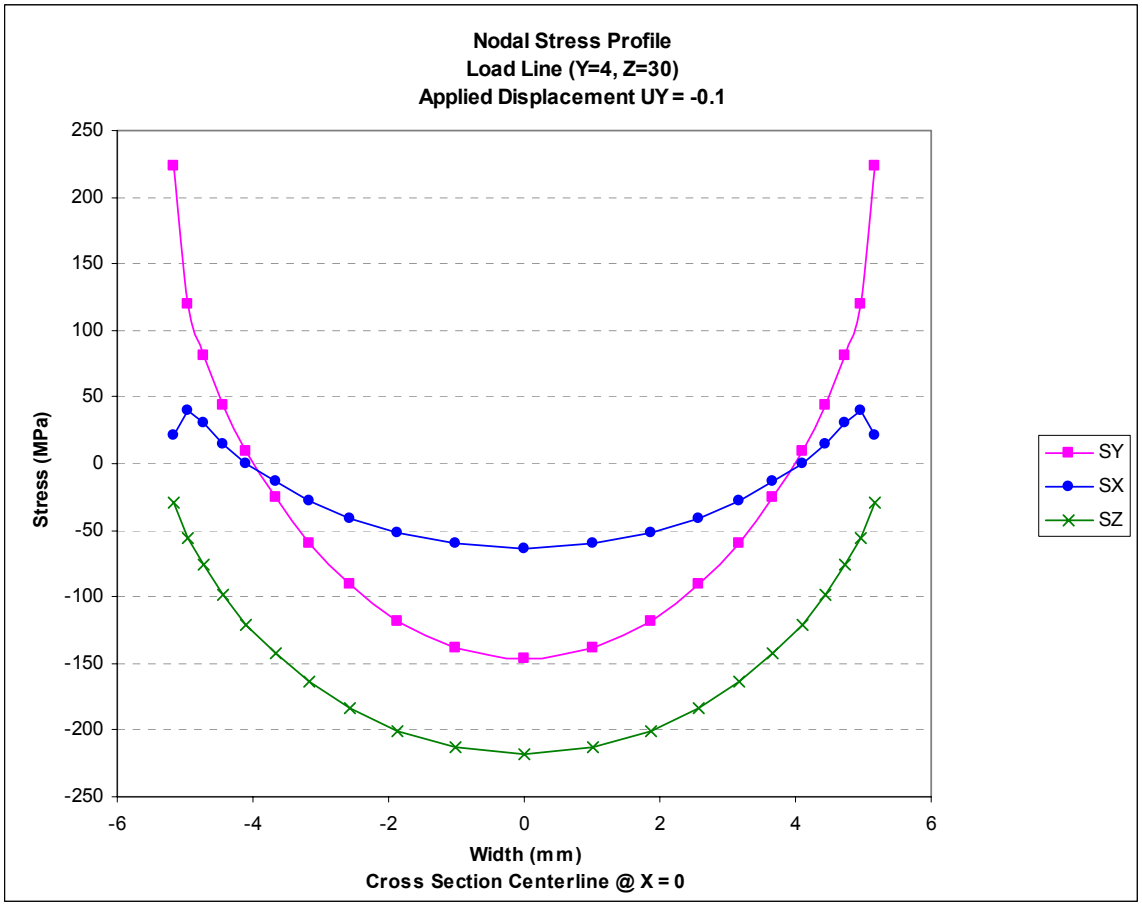

Figure 10. Nodal stresses along load support (Z = 20 mm from center) across top surface (Y = 4 mm from bottom): displacement loading.

Additionally, an independent calculation for the moment of inertia was compared to the value obtained from ANSYS. For a 1000-N load (500 N applied to each of the load lines), the closed form solution yields a maximum tensile stress of 445.66 MPa. The maximum stress obtained from the most refined mesh (see discussion) with ANSYS was 445.76 MPa. Note that the material response was assumed to be elastic throughout. Moreover, the authors wish to point out that it is not germane to the analysis of $k_V \cdot V$ and $k_A \cdot A$ that the loads and corresponding stresses are too high relative to the candidate materials undergoing consideration in the gun barrel program. For a given Weibull modulus, the parameters $k_V \cdot V$ and $k_A \cdot A$ depend only on load configuration and test specimen geometry, not on ultimate strength or elastic material properties.

In preliminary analyses, results for $k_V \cdot V$ and $k_A \cdot A$ were generated for the sectored flexure bar modeled in its entirety, i.e., the full model. In later analyses, the models were simplified via half and quarter symmetry in order to save on computational resources. For identical mesh densities, the full, half, and quarter models produced identical $k_V \cdot V$ and $k_A \cdot A$ parameters. Since the quarter symmetry models produced the least demand on computational resources, this model was used for all subsequent analyses.

Finite element analysis provides a numerical approximation of the stress field and the geometry of a component being analyzed. Since the probability of failure depends on stress and geometry and stress depends on mesh density, a mesh sensitivity study was conducted for the sectored flexure bar. Gradually increasing the mesh density allows for an asymptotic approach to estimations of the $k_V \cdot V$ and $k_A \cdot A$ parameters.

ANSYS SOLID95 elements were used to model the sectored flexure bar. A CARES surface macro was executed for each model to compute the surface of the bar for subsequent use in the calculation of $k_A \cdot A$. Five meshes were analyzed with quarter symmetry. These meshes and the corresponding number of elements are identified in table 1.

Table 1. C-ring elements according to mesh density

Mesh Density	Volume Elements	Surface Elements (CARES generated)
Most Coarse	256	208
Coarse	1,500	800
Coarse/Medium	4,480	1,552
Medium	10,500	2,410
Fine	21,000	3,800

The most coarse mesh and the fine mesh appear in figures 11 and 12. The σ_z stress (denoted SZ by ANSYS) contour plot for the quarter symmetry mesh is depicted in figure 13. This stress is not a principal stress, but the linear distribution of this stress is expected in beam bending. This contour plot is representative of the five meshes cited before. Although the magnitude of this stress is not of consequence to this discussion, the distribution of the stresses is. The stress contour plot is further confirmation that the finite element model correctly captures the expected response of the test specimen.

Figure 14 depicts a contour plot of the first principal stress. Since the CARES/Life reliability analysis will use tensile principal stresses, this figure indicates the region over which the reliability integration will be computed. Note that the tensile portion of the first principal stress "dies" in the vicinity of the outer support span. Thus, the volume outside the outer support will contribute very little to the $k_V \cdot V$ or $k_A \cdot A$ calculation.

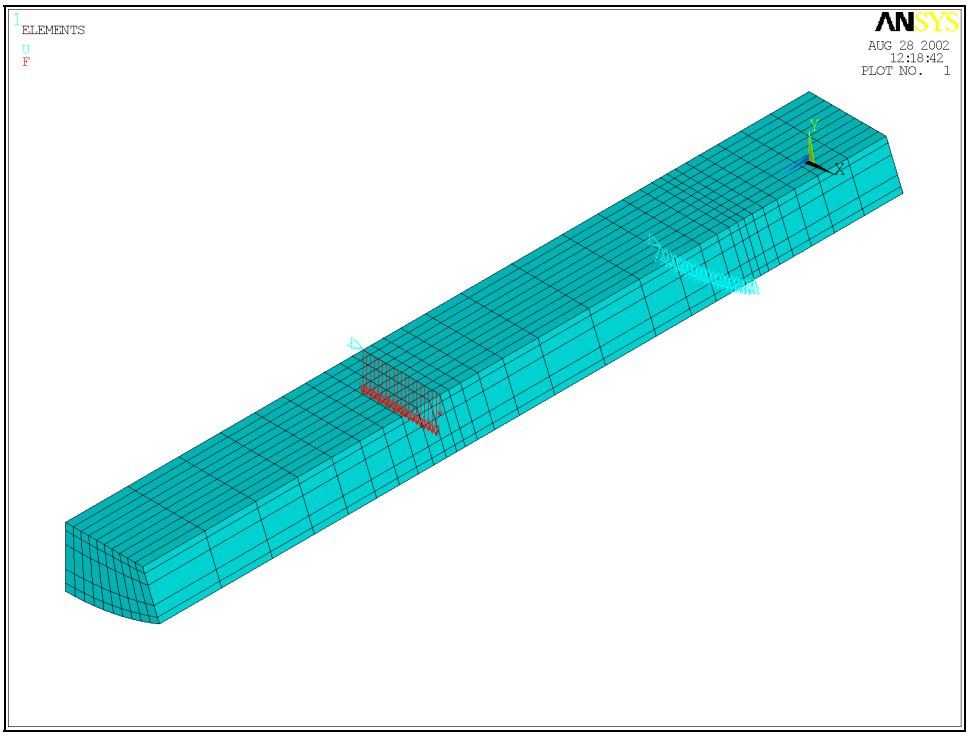

Figure 11. Most coarse quarter symmetry mesh with applied forces.

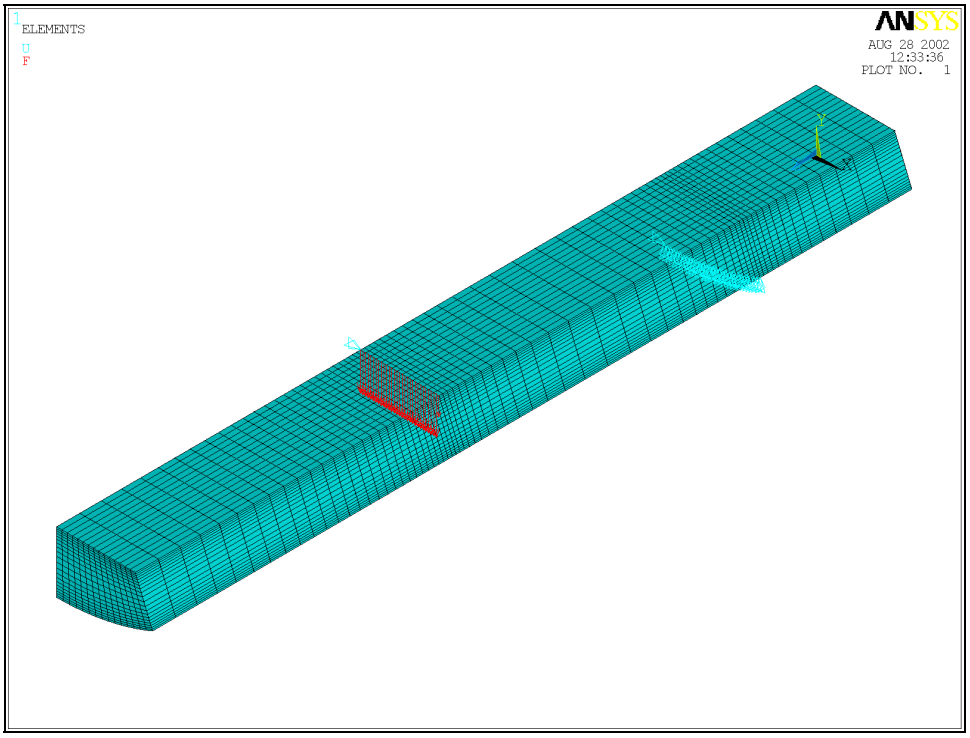

Figure 12. Most refined quarter symmetry mesh with applied forces.

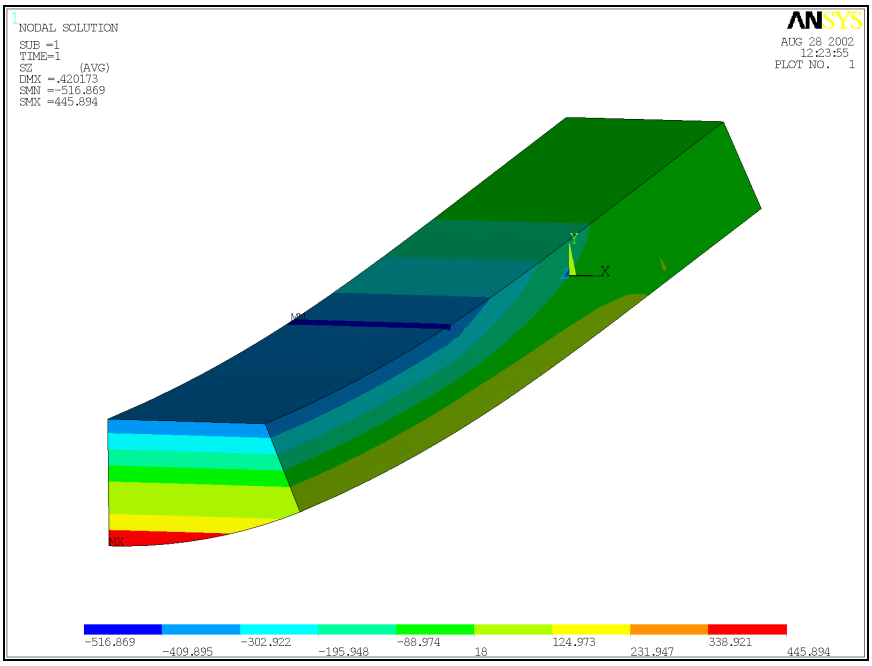

Figure 13. Z-axis stress contour plot.

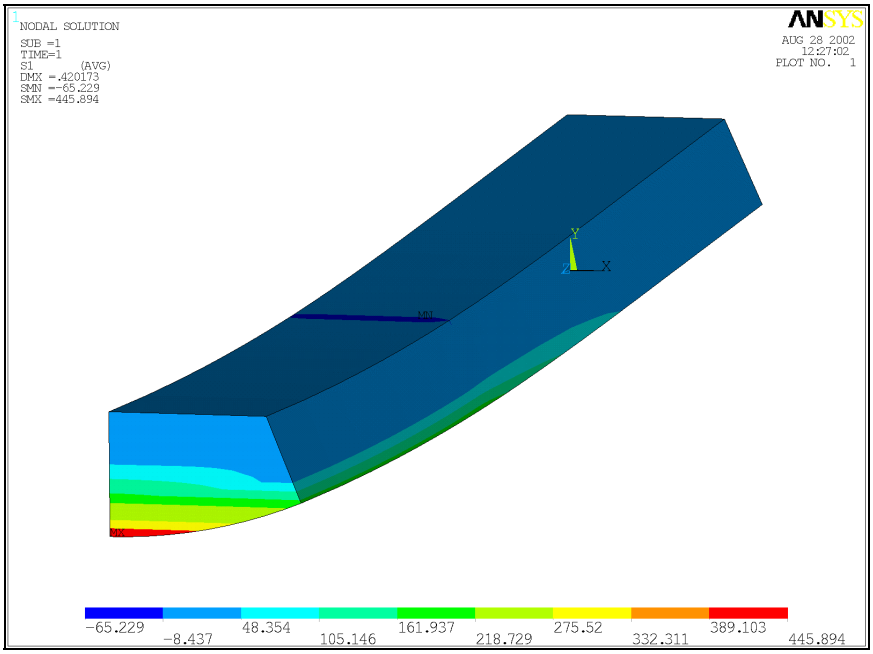

Figure 14. Principal stress contour plot.

5. C-Ring Effective Volume

Before the stress results cited previously were established, the closed form solutions for $k_V \cdot V$ and $k_A \cdot A$ cited in Jadaan et al. (1991) were considered benchmarks which the numerical approach using finite element analysis and Weibull analysis had to achieve. The closed form C-ring solution (compressive loading) for $k_V \cdot V$ is

$$k_V \cdot V = \int_V \left(\frac{\sigma_\theta}{(\sigma_\theta)_{\max}} \right)^{m_V} dV = b \; r_o^{\,m} \; f_\theta \; f_r \tag{17}$$

in which

$$f_\theta = 2 \int_0^{\pi/2} \cos^m(\theta) \, d\theta \tag{18}$$

$$f_r = \int_{r_a}^{r_o} \left(\frac{r - r_a}{r_o - r_a} \right)^m r^{1-m} \, dr \tag{19}$$

As indicated before, the computation of $k_V \cdot V$ depends on the Weibull modulus. This dependency is depicted in figure 15 where the $k_V \cdot V$ value for each mesh refinement is plotted as a function of the assumed Weibull modulus.

This plot is cited in Jadaan et al. (1991) and the relative proximity of the curves generated by numerical analysis with respect to the closed form solution is somewhat reassuring. It is interesting to note that the most coarse mesh tracks the closed form solution the best. However, a more representative graph would be the percentage difference in the numerical computation of $k_V \cdot V$ with respect to the closed form solution. This information is presented in figure 16.

In figure 16, it is quite evident that the most coarse mesh is closely tracking the closed form solution. This is counter-intuitive and leads to examining the numerical results in a manner depicted in figure 17. The graph in figure 17 indicates that the numerical computations are converging on an asymp-totic value different than the closed form solution as the mesh is refined. The results presented in figure 18 correspond to a Weibull modulus of 10, which is a value that should be representative of a material undergoing consideration in the gun barrel project.

The trends cited previously exist not only for the Weibull modulus but also for the specimen geometry. Consider the results depicted in figure 19 where the percentage difference in the numerical computation of $k_V \cdot V$ with respect to the closed form solution is graphed as a function of geometry.

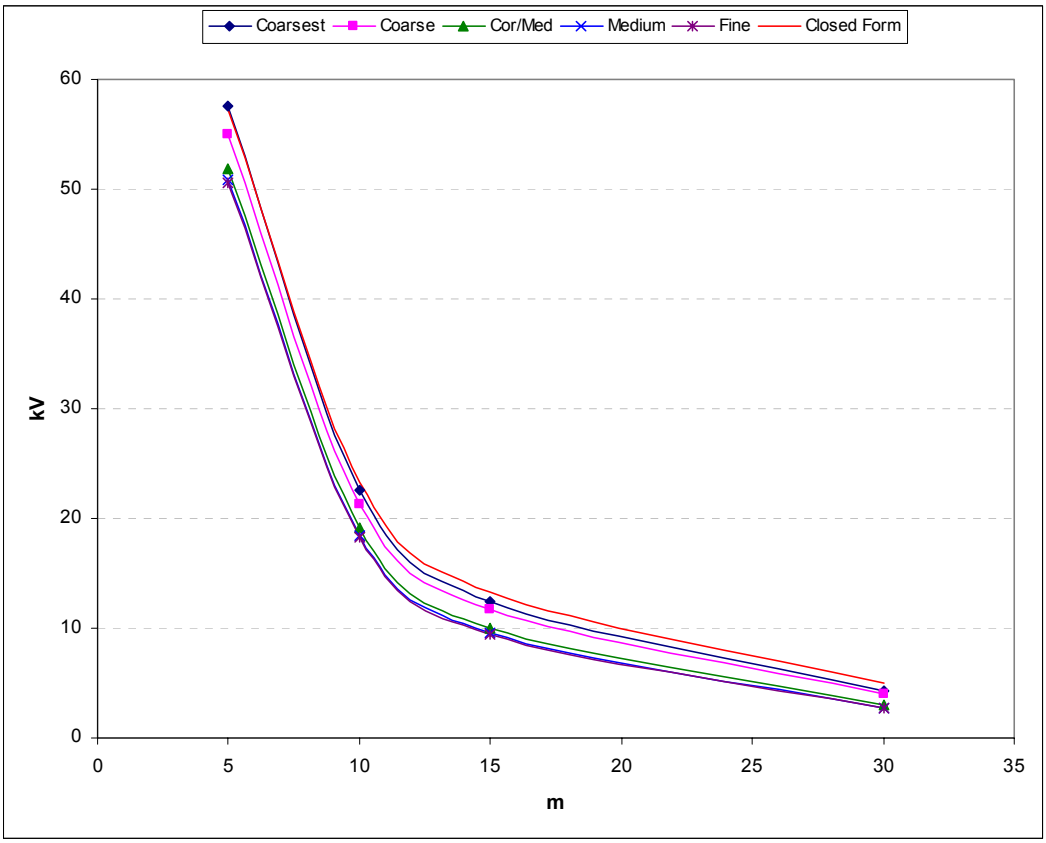

Figure 15. Effective volume ($k_V \cdot V$) as a function of the Weibull modulus and mesh.

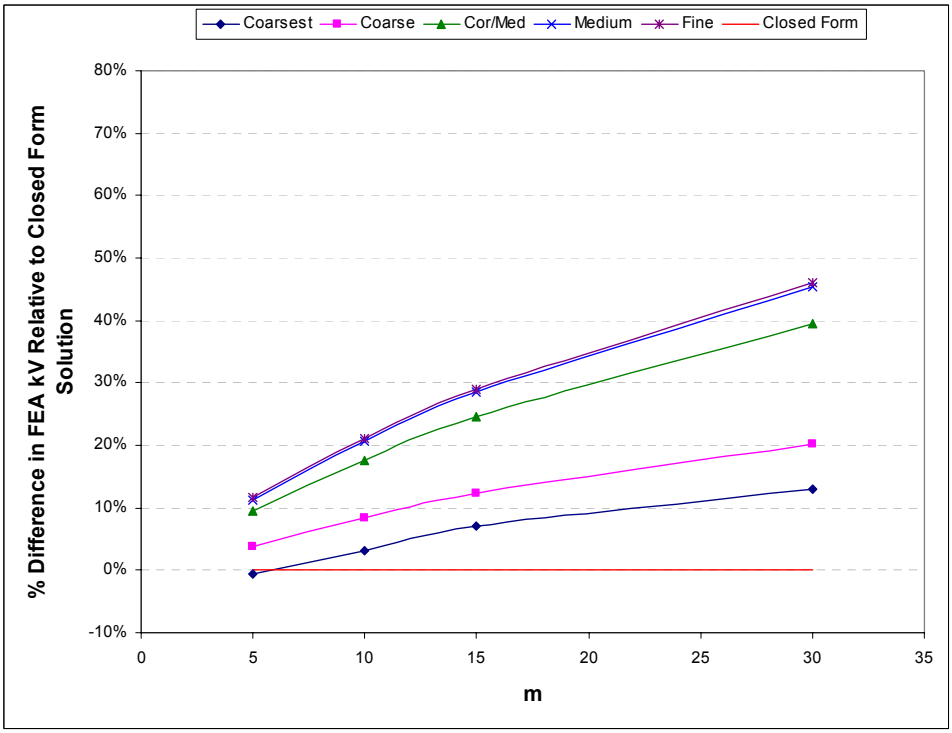

Figure 16. Percentage difference in ($k_V \cdot V$) as a function of mesh size and Weibull modulus.

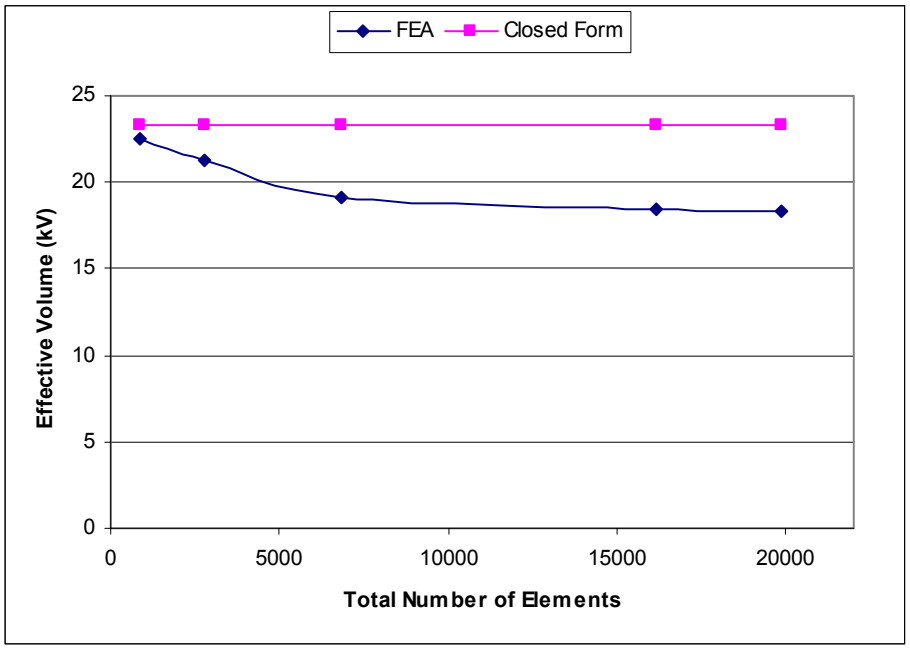

Figure 17. Effective volume as a function of mesh size for *m = 10*.

Here, the percentage difference exhibited for the most refined meshes (which represent the most accurate numerical computation) increases as the length (*b*) of the specimen increases (the inner and outer radii are held constant in this study). As long as the value of $b/(r_o - r_i)$ stays below 1, there is reasonable correlation between the two approaches.

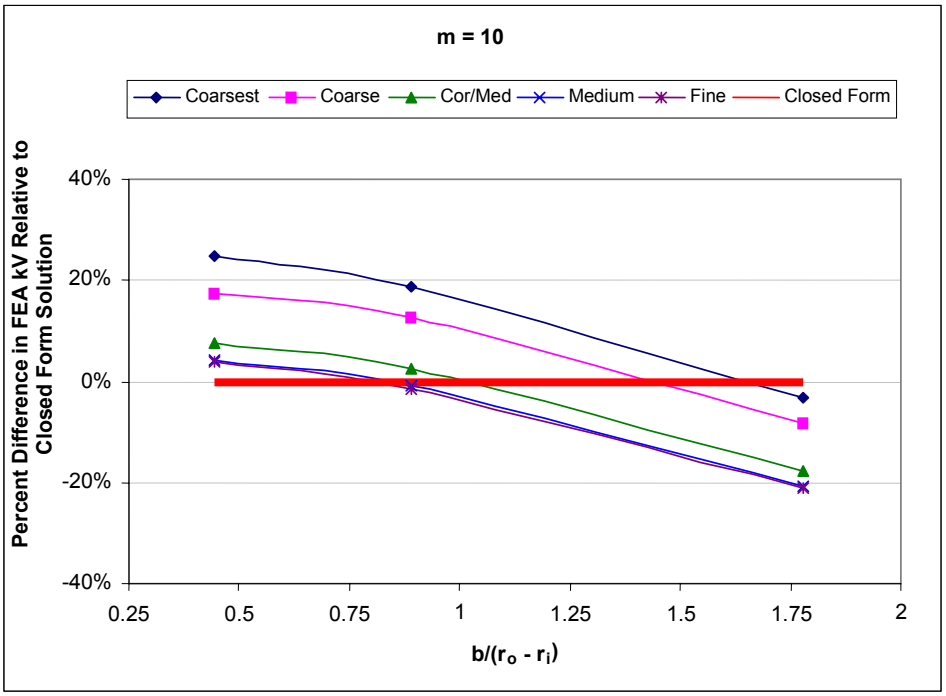

Figure 19. Percentage difference in effective volume relative to the closed form solution as a function of specimen geometry for *m = 10*.

6. C-Ring Effective Area (k_A)

The expression for $k_A \cdot A$ cited in Jadaan et al. (1991) is as follows

$$k_A \cdot A = \int_A \left(\frac{\sigma_\theta}{(\sigma_\theta)_{\max}} \right)^{m_A} dA = b\, r_o\, f_\theta + 2\, r_o^m\, f_\theta\, f_r \tag{20}$$

in which f_θ and f_r are given by equations 18 and 19.

Similar asymptotic behavior was found in the numerically generated values of the effective area parameter $k_A \cdot A$. This convergence to a value different than the closed form solution is depicted in figure 19.

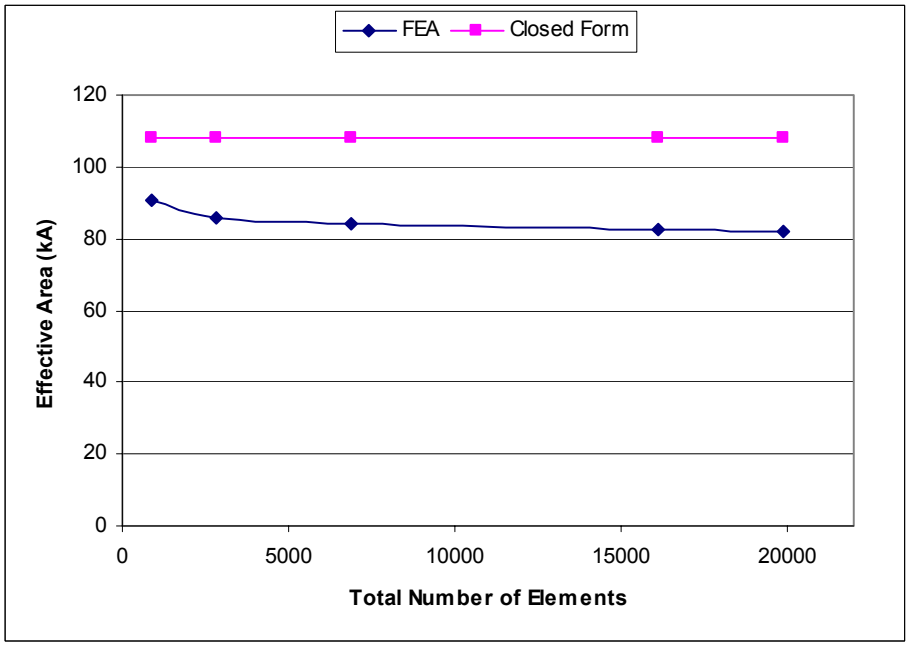

Figure 19. Effective area $(k_A \cdot A)$ as a function of mesh size for $m = 10$.

A quantitative assessment in the difference between the two values over a range of Weibull modulus values is given in figure 20.

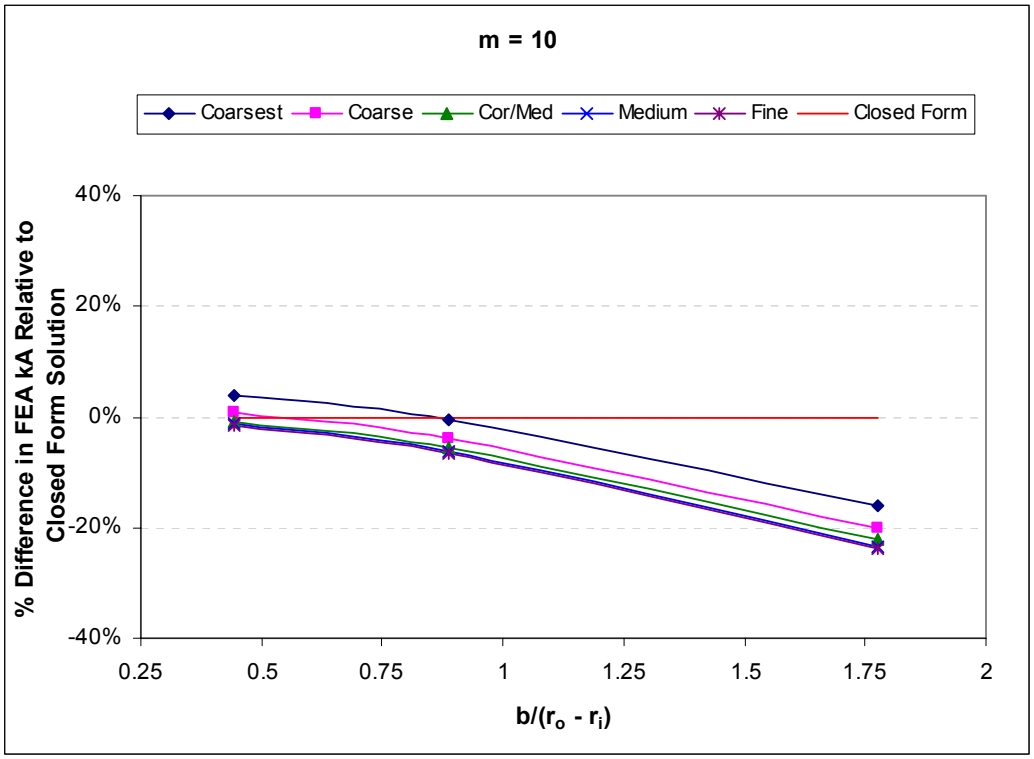

Figure 20. Percentage difference in effective area $(k_A \cdot A)$ relative to the closed form solution as a function of specimen geometry for $m = 10$.

7. Sectored Flexure Specimen Effective Volume

Closed form solutions for $k_V \cdot V$ and $k_A \cdot A$ do not exist for this specimen geometry. As indicated before, the computation of $k_V \cdot V$ depends on the Weibull modulus. This dependency is depicted in figure 21 where the $k_V \cdot V$ values for each mesh refinement are plotted as a function of the assumed Weibull modulus. The graph in figure 22 indicates that the numerical computations are converging to an asymptotic value for $k_V \cdot V$, given a Weibull modulus of 10. This value of the Weibull modulus is representa-tive of the candidate ceramic materials undergoing consideration in this program.

The asymptotic trends indicated in figure 22 were not extended to yield a single value for $k_V \cdot V$ since computational resources were exhausted at 21,000 elements using a quarter symmetry finite element model. Clearly, the asymptotic trend is there, but unlike the $k_A \cdot A$ computations where a single pronounced value is evident (see following discussion), we can only surmise a $k_V \cdot V$ value at this point. One or more mesh refinements would be necessary to confirm an asymptotic value.

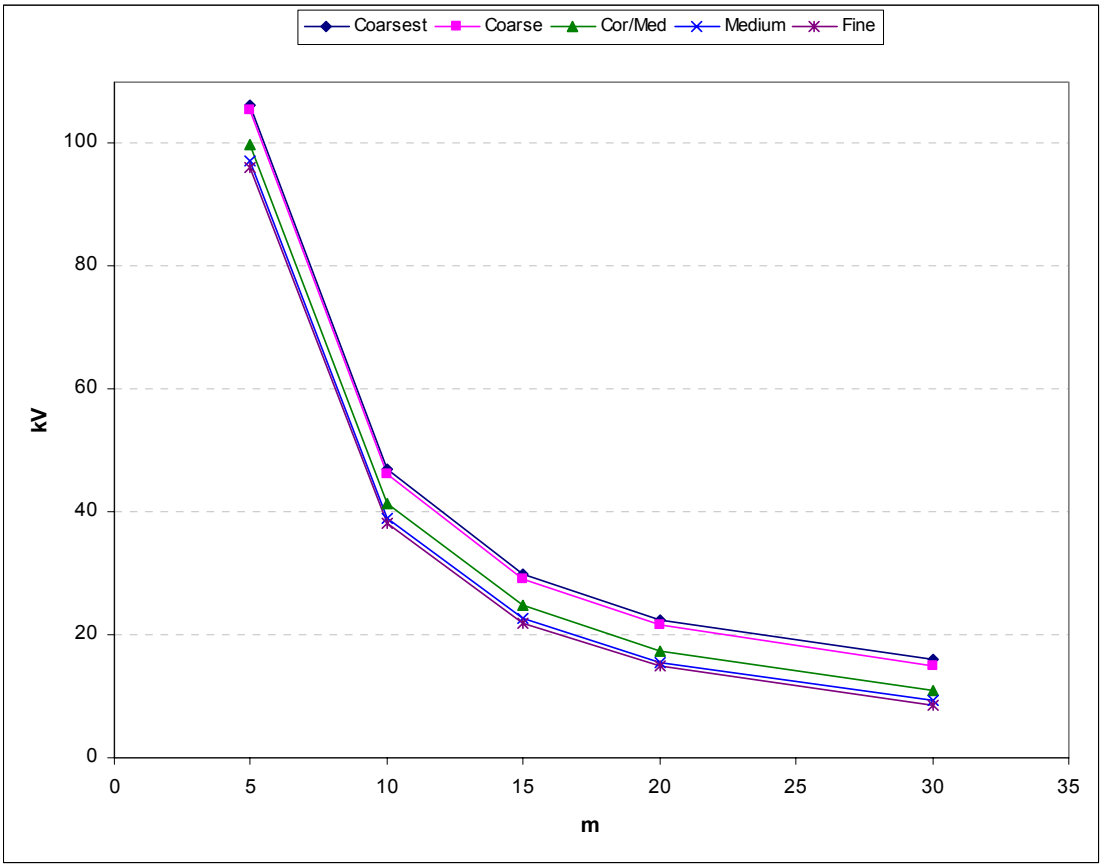

Figure 21. Effective volume ($k_V \cdot V$) as a function of the Weibull modulus and mesh density.

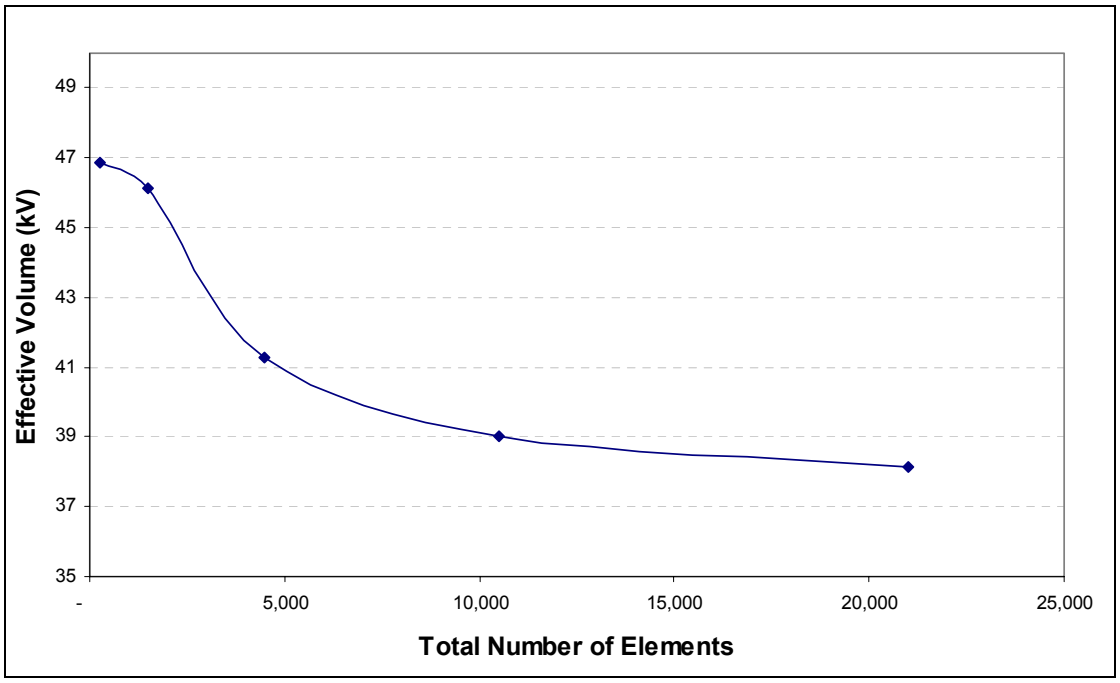

Figure 22. Effective volume as a function of mesh density for *m = 10*.

8. Sectored Flexure Specimen Effective Area

As indicated before, the computation of $k_A \cdot A$ depends on the Weibull modulus. This dependency is depicted in figure 23 where the $k_A \cdot A$ value for each mesh refinement is plotted as a function of the assumed Weibull modulus.

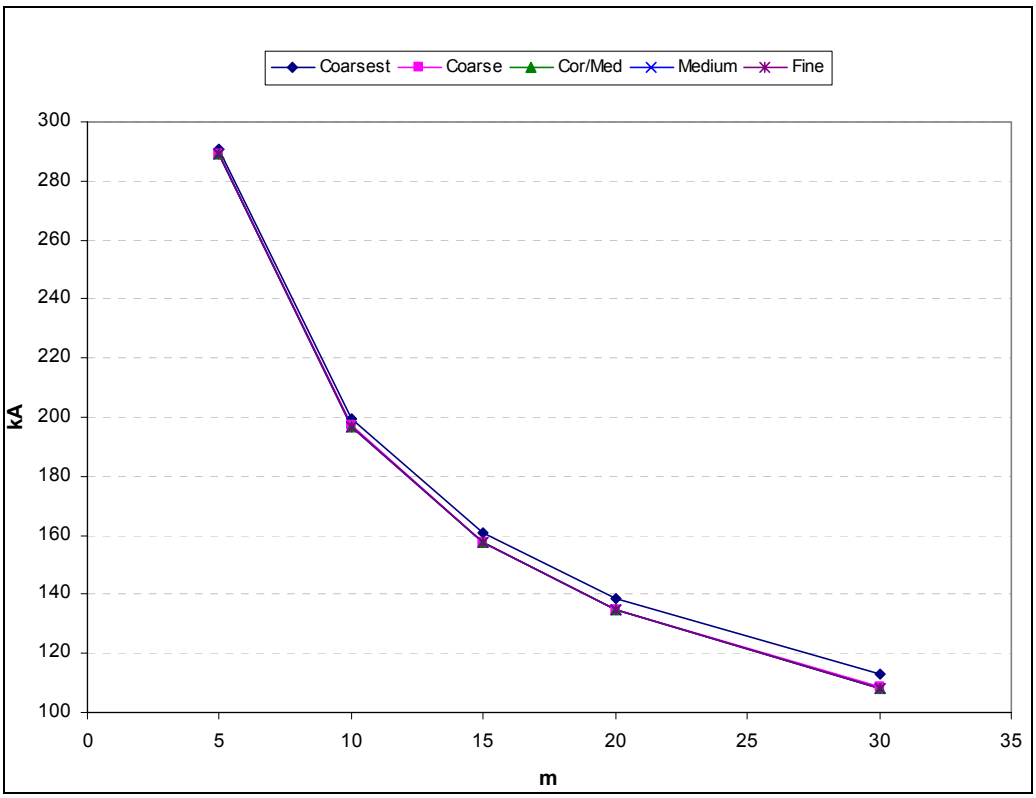

Figure 23. Effective area ($k_A \cdot A$) as a function of the Weibull modulus and mesh density.

Similar asymptotic behavior was found in the numerically generated values of the effective area parameter $k_A \cdot A$. This convergence is depicted in figure 24. Here, the asymptotic value for $k_A \cdot A$ (= 196.8 mm^2) is clearly evident.

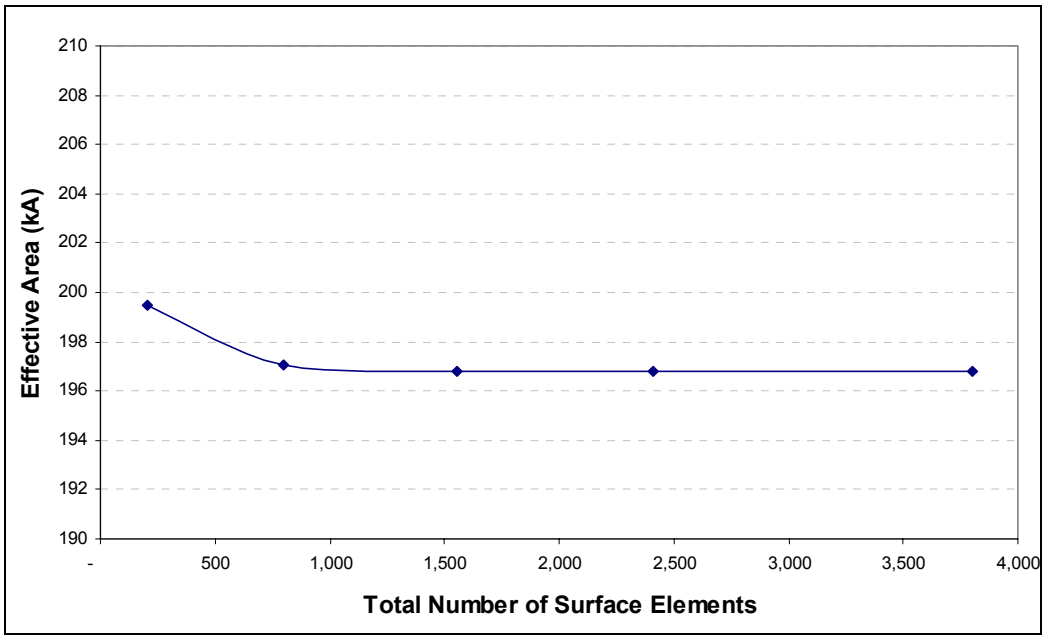

Figure 24. Effective area as a function of mesh density for $m = 10$.

9. Conclusions

The closed form solutions for $k_V \cdot V$ and $k_A \cdot A$ are not valid for the ARL C-ring specimen geometry. With the current specimen geometry, a number of finite element meshes must be evaluated to ensure asymptotic convergence of $k_V \cdot V$ and $k_A \cdot A$ for a range of Weibull modulus values. To obtain convergence with the closed form solution, the C-ring must be made more narrow. This may introduce experimental difficulties with alignment and/or stability during testing.

Consider the error introduced in component reliability calculations if the closed form solution for $k_V \cdot V$ is used to analyze failure data. The discussion that follows would also be pertinent for $k_A \cdot A$. Given the trends illustrated in the previous sections, the $k_V \cdot V$ computations are approaching theoretically correct values in an asymptotic fashion. If the closed form $k_V \cdot V$ is in error relative to a theoretically correct value, i.e.,

$$\left(k_V \cdot V\right)_{closed\ form} = Error \cdot \left(k_V \cdot V\right)_{true} \tag{21}$$

in which the subscript *"true"* refers to theoretically correct, and *Error* is an error coefficient that can be greater than or less than 1, then

$$\left(\sigma_{oV}\right)_{closed\,form} = \sigma_\theta \left(Error\right)^{1/m} \left(k_V \cdot V\right)_{true}^{1/m} \tag{22}$$

This leads to

$$\left(P_f\right)_{closed\ form} = 1 - exp\left[-\left(\frac{1}{Error}\right) \int_V \left(\frac{\sigma}{\left(\sigma_{oV}\right)_{true}}\right)^{m_V} dV \right] \tag{23}$$

or

$$\left(P_f\right)_{closed\ form} = 1 - \left(1 - \left(P_f\right)_{true}\right)^{1/Error} \tag{24}$$

whereas in equation 22

$$\left(\sigma_{oV}\right)_{true} = \sigma_\theta \left(k_V \cdot V\right)_{true}^{1/m} \tag{25}$$

is the theoretically correct Weibull material scale parameter. In terms of reliability, equation 24 can be expressed as

$$R_{closed\ form} = \left(R_{true}\right)^{1/Error} \tag{26}$$

Note that in the limit as the error coefficient becomes large (i.e., >1), the closed form reliability approaches 1, and the closed form probability of failure trends to 0. This trend is non-conservative. On the other hand, as the error coefficient approaches 0 in the limit (from 1), then the reliability and probability of failure computations obtained from the closed form approach become overly conservative.

Specifically, assume that the error coefficient assumes a value *Error = 1.25*. This value is similar to that associated with the ARL C-ring geometry for a Weibull modulus of 10. Next, assume that the component reliability based on the theoretically correct value of σ_{oV} is 0.99999, or 1 failure in 100,000. The expression given by equation 26 would then yield a component reliability of 0.999992, or 1 failure in 125,000. Thus, the component probability of failure is in error by nearly 20% (0.000008 as opposed to the theoretically correct value of 0.00001). The reliability is overestimated (and the probability of failure is underestimated), which is an non-conservative error. Thus, using an incorrect effective volume or area to analyze failure data can cascade into component design and can yield deleterious results.

The previous discussion must be tempered by the fact that loss in fidelity in calculating component reliability can be caused by several sources. These sources include (a) sampling error associated with estimating Weibull parameter from failure data, (b) experimental error in obtaining failure data, (c) using finite element analysis to obtain the stress field throughout a component, and (d) using numerical reliability algorithms to compute component probability of failure. The discussion here focused on only one source and how it affects component probability of failure. It is not the intent to imply that this type of loss in fidelity is paramount.

The rigorous interrogation of the C-ring specimen which has closed form stress solutions and effective volume and area solutions available has helped to establish an analytical protocol for the sectored flexure specimen. Because of the geometry of the sectored flexure specimen, closed form solutions are not available. Thus, the procedure established for benchmarking the C-ring specimen was applied to the sectored flexure specimen. Relative to the sectored flexure

specimen, efforts to establish an asymptotic value for $k_V \cdot V$ were not as successful as with $k_A \cdot A$. However, establishing a value for $k_V \cdot V$ may not be as important as the $k_A \cdot A$ value. Bend bars in general tend to investigate flaws near the surface. If fractography indicates the presence of surface flaws along the outside surface of the sectored flexure specimens, then there is no need to fine tune the computation of $k_V \cdot V$ for this specimen geometry.

10. References

1. Jadaan, O.M.; Shelleman, D.L.; Conway, J.C. Jr.; Mecholsky, J.J. Jr.; Tressler, R.E. Prediction of the Strength of Ceramic Tubular Components: Part I – Analysis. *ASTM Journal of Testing and Evaluation*, May 1991, 19, 181–191.
2. American Society for Testing Materials. "Standard Test Method for Ultimate Strength of Advanced Ceramics with Diametrically Compressed C-Ring Specimens at Ambient Temperature" in *Annual Book of Test Standards*; ASTM Standard C 1323-96, Vol. 15.01; West Conshohocken, PA, 2004.
3. Timoshenko, S.P.; Goodier, J.N. *Theory of Elasticity*; McGraw-Hill, Inc., Third Edition, New York, 1970.

NO. OF
COPIES ORGANIZATION

* ADMINISTRATOR
DEFENSE TECHNICAL INFO CTR
ATTN DTIC OCA
8725 JOHN J KINGMAN RD STE 0944
FT BELVOIR VA 22060-6218
*pdf file only

1 DIRECTOR
US ARMY RSCH LABORATORY
ATTN IMNE ALC IMS MAIL & REC MGMT
2800 POWDER MILL RD
ADELPHI MD 20783-1197

1 DIRECTOR
US ARMY RSCH LABORATORY
ATTN AMSRD ARL CI OK TL TECH LIB
2800 POWDER MILL RD
ADELPHI MD 20783-1197

2 OAK RIDGE NATL LAB
STRUCTURAL CERAMICS GROUP
ATTN A A WERESZCZAK MS 6068
M FERBER MS 6068
PO BOX 2008 BLDG 4515
OAK RIDGE TN 37831-6068

2 OAK RIDGE NATL LAB
HIGH TEMPERATURE MATERIALS LAB
ATTN DAVE STINTON MS 6069
EDGAR LARA CURZIO MS 6069
PO BOX 2008 BLDG 4515
OAK RIDGE TN 37831-6069

1 GATEWAY MATERIALS TECH INC
ATTN STEPHEN T GONCZY
221 SOUTH EMERSON
MOUNT PROSPECT IL 60056

3 NASA GLENN RSCH CTR
LIFE PREDICTION BRANCH MS 49 7
ATTN J A SALEM J P GYEKENYESI
N N NEMETH
21000 BROOKPARK ROAD
CLEVELAND OH 44135

1 UNIV OF DETROIT-MERCY
ATTN MICHAEL G JENKINS
4001 W MCNICHOLS RD
PO BOX 19900
DETROIT MI 48219-0900

1 SAINT GOBAIN ABRASIVES
ATTN KRISTIN BREDER
ONE BOND ST PO BOX 15008
WORCESTER MA 01615

NO. OF
COPIES ORGANIZATION

1 LLNL DEFENSE TECHNOLOGIES
ADVANCED ENGINEERING ANALYSIS
ATTN ROBERT A RIDDLE
PO BOX 808 L 125
LIVERMORE CA 94551

1 3M ADV MATERIALS TECH CTR
ATTN DOUGLAS J PYSHER
BLDG 201 4 N 01
ST PAUL MN 55144-1000

1 NATL INST OF STANDARDS & TECHNOLOGY
ATTN GEORGE D QUINN
STOP 852 CERAMICS DIV BLDG 223
GAITHERSBURG MD 20899-852

1 UNIV OF WISCONSIN PLATTEVILLE
COLLEGE OF ENG MATH SCIENCE
ATTN OSAMA JADAAN
150 OTTENSMAN HALL
PLATTEVILLE WI 53818

1 GENERAL ELECTRIC COMPANY
ATTN CURT JOHNSON
BLDG K 1 ROOM MB 161
PO BOX 8
SCHENECTADY NY 12301

1 PENNSYLVANIA STATE UNIV
ATTN AL SEGALL
212 EARTH & ENG SCIENCE BLDG
UNIVERSITY PARK PA 16802

1 PENNSYLVANIA STATE UNIV
ATTN JOHN HELLMANN
124 STEIDLE BLDG
UNIVERSITY PARK PA 16802

ABERDEEN PROVING GROUND

1 DIRECTOR
US ARMY RSCH LABORATORY
ATTN AMSRD ARL CI OK (TECH LIB)
BLDG 4600

2 AEC
ATTN CSTE AEC TS M&S R MIRABELLE
CSTE AEC CCEW P CRISE
BLDG 4120

4 AMSAA
ATTN AMXSY CA W BROOKS J CARR
G DRAKE R FRANKLIN
BLDG 367

NO. OF
COPIES ORGANIZATION

2 DIRECTOR
US ARMY RSCH LABORATORY
ATTN AMSRD ARL SL BB M ENDERLEIN
AMSRD ARL SL EA W PEEL
BLDG 247

1 DIRECTOR
US ARMY RSCH LABORATORY
ATTN AMSRD ARL WM B A HORST
BLDG 4600

1 DIRECTOR
US ARMY RSCH LABORATORY
ATTN AMSRD ARL WM BA D LYON
BLDG 4600

1 DIRECTOR
US ARMY RSCH LABORATORY
ATTN AMSRD ARL WM BC P PLOSTINS
BLDG 4600

1 DIRECTOR
US ARMY RSCH LABORATORY
ATTN AMSRD ARL WM BD B FORCH
BLDG 4600

11 DIRECTOR
US ARMY RSCH LABORATORY
ATTN AMSRD ARL WM BF P HILL
J LACETERA B HAUG
S WILKERSON J WALD J WALL
R PEARSON W OBERLE M FIELDS
G SAUERBORN P FAZIO
BLDG 390

1 DIRECTOR
US ARMY RSCH LABORATORY
ATTN AMSRD ARL WM EG E SCHMIDT
BLDG 4600

1 DIRECTOR
US ARMY RSCH LABORATORY
ATTN AMSRD ARL WM M J MCCAULEY
BLDG 4600

1 DIRECTOR
US ARMY RSCH LABORATORY
ATTN AMSRD ARL WM MA S MCKNIGHT
BLDG 4600

NO. OF
COPIES ORGANIZATION

18 DIRECTOR
US ARMY RSCH LABORATORY
ATTN AMSRD ARL WM MB J SWAB
J BENDER L BURTON
T BOGETTI R CARTER
K CHO W DEROSSET
R DOWDING W DRYSDALE
R EMERSON D HOPKINS
R KASTE L KECSKES
B POWERS D SNOHA
J SOUTH M STAKER
J TZENG
BLDG 4600

1 DIRECTOR
US ARMY RSCH LABORATORY
ATTN AMSRD ARL WM MC M MAHER
BLDG 4600

2 DIRECTOR
US ARMY RSCH LABORATORY
ATTN AMSRD ARL WM MD J ADAMS
W ROY
BLDG 4600

1 DIRECTOR
US ARMY RSCH LABORATORY
ATTN AMSRD ARL WM TC R COATES
BLDG 309

1 DIRECTOR
US ARMY RSCH LABORATORY
ATTN AMSRD ARL WM TE B RINGERS
BLDG 1116A